Li, Q., Deng, L., Kim, J-K., Zhu, Y. Q., Holmes, S. M., Perez-Page, M., & Eichhorn, S. J. (2017). Growth of carbon nanotubes on electrospun cellulose fibers for high performance supercapacitors. *Journal of the Electrochemical Society*, *164*(13), A3220-A3228. https://doi.org/10.1149/2.1181713jes

Growth of Carbon Nanotubes on Electrospun Cellulose Fibres for High Performance Supercapacitors

Qiang Li[1], Libo Deng[2], Jang-Kyo Kim [3], Yanqiu Q. Zhu[1], Stuart M. Holmes[4], Maria Perez-Page[4], Stephen J. Eichhorn [1*]

[1] College of Engineering, Mathematics and Physical Sciences, Harrison Building, North Park Road, University of Exeter, EX4 4QF, UK.

[2] College of Chemistry and Environmental Engineering, Shenzhen University, Shenzhen 518060, PR, China.

[3] Department of Mechanical and Aerospace Engineering, The Hong Kong University of Science and Technology, Clear Water Bay, Kowloon, Hong Kong.

[4] School of Chemical Engineering & Analytical Science, University of Manchester, Oxford Road, Manchester, M13 9PL UK.

ABSTRACT We report the production of cellulose-derived hybrid carbon nanofibre (CNF)/ carbon nanotubes (CNTs) electrodes for the fabrication of high-performance supercapacitors. The CNTs were grown via a floating catalyst chemical vapor deposition (CVD) method on the top surface of electrospun cellulose-derived CNFs. The morphology of these hybrid CNF/CNTs fibrous structures was investigated using scanning electron and transmission electron microscopy. The development of these carbon structures was characterized using Raman spectroscopy. The electrochemical performance of the devices including cyclic voltammetry (CV), galvanostatic charge/discharge (GCD), electrochemical impedance spectroscopy measurements (EIS), and electrochemically stability was carried out. These hybrid CNF/CNTs electrodes had a high value of specific capacitance of 149 F g^{-1} at a current density 0.5 A g^{-1}, an increase of 15 % compared with pristine CNFs. The BET specific surface area increases from 712 m^2 g^{-1} to 1211 m^2 g^{-1} from pristine CNFs to hybrid CNF/CNTs, leading to a specific capacitance (per unit area) of ~170 mF cm^{-2}. These supercapacitors also retain 90% of the original capacitance over 1000 cycles, showing an excellent stability. This method

* Present Address: Bristol Composites Institute (ACCIS), University of Bristol, Queen's Building, University Walk, Bristol BS8 1TR, United Kingdom. Email: s.j.eichhorn@bristol.ac.uk

of supercapacitor electrode production is suggested as a basis to convert a sustainable cellulosic material into a useful energy storage material.

KEYWORDS: supercapacitor, cellulose, nanocomposite, CNT

1. Introduction

As demand continuously increases in numerous industries such as portable electronics and new 'green' vehicles, energy storage devices such as supercapacitors should be further developed to provide increased performance. These improvements will be better understood by investigating electrode materials at the nanoscale, where a large surface area provides an increased charge mobility and a network which can interact well with the dielectric. Supercapacitors, also known as electrochemical double layer capacitors (EDLC), store energy by accumulation of the electrostatic charges at the electrode interfaces. They stand out among the energy storage devices such as lithium ion batteries and fuel cells owing to their high power density, fast charge/discharge mobility, and good life cycle stability.[1] The high performance of EDLC benefit from the extremely small separation (molecular scale) of charges generated at the interface between the electrode and electrolyte. Electrode materials for these devices typically aim to maximise surface area in order to store more charge than traditional parallel-plate capacitors.[2] Carbon nanofibres are particularly promising for the fabrication of electrodes owing to their relatively high surface area, pore size distribution, high electrical conductivity, good mechanical properties, and excellent cyclic stability.[3]

Cellulose nanofibres have a huge potential for the production of carbon fibre based electrodes to complement or replace commercial oil-based polyacrylonitrile (PAN) precursors. This potential arises because they are inexpensive, renewable, highly crystalline and abundant in nature.[4] When performing thermal treatment of cellulose fibres, at elevated temperatures above 400 °C, the carbonaceous structure is developed from the cellulose precursor by the process involving physical removal of water, dehydration, scission of glycosidic linkages, and aromatization.[5]

Electrospinning is a simple and continuous approach to generate nanofibres by applying electrostatic forces to a polymer solution.[6] Electrospinning is capable of producing fibres with large surface to volume ratios.[7] Although the application of electrospun fibres has largely enhanced the electrochemical properties of supercapacitors, a further approach to hybridise the

surface with the presence of other nanomaterials may realise the full potential of the storage ability of the ions in the electrolyte.[8]

Carbon nanotubes (CNTs), first discovered by Iijima,[9] have been intensively investigated as additives for the production of supercapacitors in recent years.[10-13] As the diameters of CNTs are much smaller than typical electrospun CNFs, their incorporation with CNFs can achieve a significant increase in the surface area of the electrodes, subsequently increasing their electrochemical performance. Deng *et al.* have reported that by adding 6 wt.% CNTs into an electrospun cellulose acetate solution, the subsequently activated CNFs led to an increase of 38% of the specific electrochemical capacitance.[14] Deng *et al.* used an approach whereby CNTs were added to the electrospinning solution[14], whereas we propose the in situ production of nanotubes on the surface of the spun fibres. The concentration of CNTs within the fibres in Deng's work was limited in this case by the viscosity of the electrospun solution such that it hindered any further improvement of capacitive performance.[14] In the present work we show further increase in the specific capacitance, but also a method to form hybrid structured fibres for incorporation into structural capacitors and hierarchical composites.[15, 16]

Chemical Vapor Deposition (CVD) is an excellent method to grow CNTs on a CNF substrate. In general, it is a fast and easy method in comparison to other approaches for the incorporation of CNTs on CNFs, e.g. dispersion of CNTs in the electrospun polymeric solution[14] or physically grafting CNTs onto the surface of CNFs.[17] CVD processes that have been used to grow CNTs on CNFs include a floating catalyst approach,[18] grafting the catalyst by simply dipping CNFs into the solution containing the catalyst,[19] and encapsulating the catalyst nanoparticles into the CNFs by electrospinning.[20, 21] Among these methods, the floating catalyst approach is considered to be the most convenient and size-controllable processing route to make CNF/CNTs. In the present study, CNF/CNTs composites were made by producing in situ grown CNTs on the top surface of electrospun cellulose derived activated carbon nanofibres. The resulting hierarchical composite fibres showed much better electrochemical performance over the plain CNFs. The approach represents a new way of making capacitive electrodes, and offers a route to transform a sustainable material (cellulose) into energy storage devices that could have wide-ranging applications.

2. Experimental

2.1. Materials preparation

Cellulose acetate (CA, average M_n = 100,000 g mol^{-1}) was supplied by Fisher-Scientific (Loughborough, UK). Acetone, N,N-dimethylacetamide (DMAc), sodium hydroxide (NaOH), and potassium hydroxide (KOH) were purchased directly from Sigma-Aldrich (Dorset, UK). The polymeric solution used for electrospinning was made by dissolving 20 wt.% CA powder in a mixed solution of acetone and DMAc (2:1 w/w). The solution was stirred using a magnetic stirrer overnight at room temperature.

2.2. Electrospinning and deacetylation of fibres

Electrospinning was carried out using the prepared CA solution. The spinning conditions were a voltage of 14 kV, a flow rate of 1 mL h^{-1} and a needle tip-to-collector distance of 14 cm. The electrospinning process was continued for 3 hours and the electrospun CA nanofibres were deposited onto an aluminium foil collector to form a fibrous mat. These fibrous mats were then deacetylated in a 0.05 M NaOH aqueous solution for 48 h to allow regeneration into pure cellulose fibres, and were then fully rinsed with deionized water until neutral, and finally air dried.

2.3. Pyrolysis of regenerated cellulose and Chemical Vapor Deposition (CVD)

Stabilization and carbonization were undertaken in a high temperature tube furnace (Elite TSH16 furnace). Stabilization was firstly carried out for regenerated cellulose fibres by ramping the furnace from room temperature to 240 °C at a heating rate of 5 °C min^{-1} in air, followed by dwelling for 60 minutes. The stabilized fibres were then carbonized by ramping the temperature from 240 °C to 900 °C at a ramping rate of 10 °C min^{-1}, followed by dwelling for 30 minutes in an argon atmosphere. The carbonized fibres were denoted as CF900.

CF900 fibres were pre-located in the hot zone of the quartz tube in a CVD furnace, as shown in Figure 1. The quartz tube had an inner diameter of 26 mm. The furnace was then heated to the required temperature of 800 °C. A mixed solution of 0.01 g ml^{-1} of ferrocene in styrene was fed into the quartz tube via a pump-controlled syringe at a flow rate of 0.8 cm^3 min^{-1}. The styrene acts as a carbon source and ferrocene as a catalyst to promote the CNT growth. The syringe end located inside of the quartz tube was maintained at 200 °C, which is higher than

the ferrocene sublimation temperature (140 °C) and the styrene boiling point (145 °C) to ensure a ferrocene/styrene vapor was being produced. The mixed vapor was fed with a mixture of flowing argon-hydrogen gas of ratio (v:v = 1:1) at a flow rate of 200 cm^3 min^{-1} into the reaction zone of the heated quartz tube. The reaction was carried out for 25 minutes. The resulting composite structure, produced by the combination of carbonised electrospun cellulose fibres (CF900) and CNTs is subsequently denoted as CF900/CNTs.

2.4 Activation of carbon fibres

For KOH activation of the electrode materials, 0.005 g mL^{-1} KOH aqueous solution was deposited on both sides of the CF900 and CF900/CNTs fibre mats. The mats were then dried at 60 °C to remove the water. KOH therefore remained on the surface of the fibres. The process of deposition of KOH solution and drying were repeated until the ratio of KOH and CF900 or CF900/CNTs was 1:2 (g/g). Activation was then performed in a tubular furnace by heating to 700 °C from room temperature at a heating rate of 2 °C min^{-1} in an Ar atmosphere, followed by a dwell time of 45 minutes. The activated electrode materials were then dipped into a 4.8 M aqueous nitric acid solution to remove as much of the remaining catalyst as possible and other impurities. Then these samples were rinsed and dried.

2.5 Characterisation of fibres

A scanning electron microscope (SEM) (HITACHI S3200N SEM-EDS) with a voltage of 20 kV was utilized to observe the morphologies of the carbon fibres and the CNTs. The CF900/CNTs fibre mats were sonicated in water for 15 minutes and deposited onto transmission electron microscopy (TEM) grids to examine the nanostructures and the morphology of CNTs with CNFs. Raman spectroscopy was utilized to characterize the electrospun CA and cellulose fibres, and the carbonized CNFs and CVD grown samples. Spectra were obtained using a 532 nm laser coupled to a Renishaw RM1000 spectrometer. A Leica CCD detector was used to record the spectral output. The laser spot size was ~1-2 µm, and the power was ~1 mW when the laser was focused on the sample using a 50× objective microscope lens. The specific surface area was calculated by Brunauer-Emmett-Teller (BET) method. The micropore volume (V_{micro}) and micropore area (S_{micro}) were obtained by using the t-plot method, while the mesopore volume (V_{meso}) and mesopore area (S_{meso}) were estimated by the Barrett-Joyner-Halenda (BJH) method. The total pore volume (V_{tot}) was measured by the nitrogen adsorption volume at the highest relative pressure. Pore size distribution was

determined by the Non-local Density Functional Theory (NLDFT). Thermogravimetric analysis (TGA) was performed by heating activated CF900/CNTs at a heating rate of 10 °C min^{-1} from room temperature to 700 °C in air.

A symmetric 'coin cell' supercapacitor was fabricated by assembling two pieces of activated CNF electrodes with GF/A Whatman filter paper as a separator, and a 6 mol L^{-1} aqueous KOH as the electrolyte (a picture of a typical coin cell supercapacitor is shown in Figure S1, Supplementary Information). The areal mass for each electrode of CF900 and CF900/CNTs were 0.8 mg cm^{-2} and 1.1 mg cm^{-2}, respectively. A cyclic voltammetry (CV) test was performed on a CHI600C electrochemical workstation (CEW) at a scan rate 10 mV s^{-1} for both CF900 and CF900/CNTs electrodes. To test the rate performance of the composite capacitor (CF900/CNTs), a voltage range between 0 and 0.8 V was used for the CV measurements at four different scan rates (10, 50, 100 and 200 mV s^{-1}), and galvanostatic charge/discharge (GCD) tests were performed at three different current densities (0.5, 2, and 10 A g^{-1}). Electrochemical impedance spectra (EIS) were obtained at a constant perturbation amplitude of 5 mV at frequencies ranging from 0.01 Hz to 100 kHz. Electrochemical stability tests for both CF900 and CF900/CNTs were also performed by chronopotentiometry on the CEW for 1000 cycles at a current density of 2 A g^{-1}. Values of specific capacitance C_{SP} for each electrode were calculated from the GCD curves using the equation[22]

$$\boldsymbol{C_{sp} = 2I/\left(m(\mathrm{d}V/\,\mathrm{d}t)\right)} \qquad (\mathbf{1})$$

where dV is the voltage difference, dt is the discharge duration, I is the current and m is the average mass of the electrodes.

3. Results and discussion

3.1. Processing and morphology of CNF/CNTs

The effect of CVD temperature was investigated by comparing two operating temperatures; namely at 800 and 900 °C. When performing CVD at 800 °C, CNTs are obtained without the appearance of other carbon impurities, e.g. amorphous carbon. A thick CNT layer was formed on the surface of the CNFs (Figure 2a). Many long CNTs were observed to be entangled at the circumferential surfaces of CNFs. TEM images (Figures 2b and 2c) give evidence for the formation of multiwalled CNTs. Some round Fe nanoparticles were found to be encapsulated

at the CNT tip with a similar diameter as the outer wall of the CNT; a typical example is shown in Figure 2c. This observation reveals that the growth mechanism of the CNTs follows a "tip-growth model", which only takes place when the catalyst is weakly attached to the substrate with an acute contact angle.[23] The presence of Fe nanoparticles may also reduce the electrochemical efficiency of the supercapacitor devices. To obtain various CNT contents in the samples, CVD duration time and speed of feeding the catalysts/carbon source are two of the most appropriate approaches. In addition, the concentration of Argon and H_2 is also adjustable to change the CNT content. These parameters could be investigated in future work to optimize the growth of the CNTs.

In contrast, the amorphous carbon and clusters thereof are clearly observed when using a CVD temperature of 900 °C (Figure 2d). The amorphous carbons are larger than the CNTs in diameter. In the CVD process, ferrocene as the catalyst, first decomposes into Fe nanoparticles at 900 °C facilitated by H_2.[24] Styrene, as a carbon source, decomposes into carbon atoms, followed by diffusion into the Fe nanoparticles. However, it is difficult for diffused carbon atoms to precipitate CNTs on the large catalyst particles and therefore they form iron carbide (Fe_3C) along with amorphous carbon, or 'carbon balls' instead.[25] The amorphous carbon then coats the Fe nanoparticles causing so-called catalyst 'poisoning', clearly seen in Figure 2e, resulting in catalyst deactivation to impede the growth of CNTs. Other studies have also shown that amorphous carbon appears at temperatures above a window of 800 to 825 °C.[26] Also, the relationship between growth temperature and the density of CNTs on carbon fibre surfaces has been previously investigated.[27] This previous work suggests that a very low number of CNTs form at 700 °C due to the low solubility of carbon in the iron catalyst at temperatures lower than the carbon-iron eutectic temperature of 723 °C.[27] The density of CNTs experiences a substantial increase at 750 °C and reaches the highest level at 800 °C. Thus, the most suitable temperature window is 750 - 825 °C for the growth of pure CNTs in a floating catalyst CVD process.

3.2. Structural feature of fibres characterized by Raman spectroscopy

Typical Raman spectra for the as-spun CA and deacetylated CA fibres are shown in Figure 3a. After deacetylation, an intense peak appeared at ~1095 cm^{-1}, which is attributed to the C-O ring and glycosidic linkage stretching modes, indicating the presence of cellulose.[28] However, this peak is absent in the spectra for the original CA fibres. Additionally, three peaks located

at ~898 cm^{-1}, ~1262 cm^{-1} and ~1462 cm^{-1} are attributed to the cellulose II crystal lattice.[29, 30] A much broader and significant peak also appeared at ~1374 cm^{-1} because of the $\delta(CH_2)$ mode.[29]

Raman spectra of CF900 and CF900/CNTs are presented in Figure 3b. These Raman spectra were fitted using a 2-peak Lorentzian curve to determine their peak positions and the intensity ratio (I_D/I_G) of the G and D bands was obtained. In a phonon dispersion mode, the G band is attributed to the doubly degenerate in-plane transverse (iTO) mode and the longitudinal (LO) phonon mode with E_{2g} symmetry at the Γ point inside the first Brillouin zone (BZ).[31] The G band in the Raman spectrum is found to be located at ~1590 cm^{-1} for sp^2 carbon hexagonal in-plane bond-stretching motions. The D band is assigned to a non-degenerate phonon coming from the iTO branch at the K-point with A_{1g} symmetry.[31] The D band is located at ~1350 cm^{-1} and results from the vibrations of carbon atoms that are located at the graphite sheet edge and relates to defects in sp^2 carbon structures, including edge dislocations, vacancies, and crystal edges.[31] The 2D band is attributed to 2 phonons near the K-point,[32, 33] located at ~2700 cm^{-1} which is caused by an overtone of the D band and is observed in Raman spectra for multi-walled CNTs.[34]

The ratio of the intensities of the D and G bands (I_D/I_G) is widely used to characterize the disorder and the degree of crystallinity in graphitic materials. The evolution of disorder is typically quantified using the Tuinstra–Koenig (TK) equation[35] described by the equation

$$\boldsymbol{I_D/I_G = C(\lambda)/L_a} \qquad (\mathbf{2})$$

The value of C (λ) has been reported to be 4.4 nm for a laser wavelength λ = 514 nm;[36] this constant depends on the excitation laser wavelength used.[37] L_a represents the in-plane crystalline size in graphitic materials.

Ferrari and Robertson have however found that the TK equation is invalid when L_a is smaller than 2 nm.[36] They proposed a new modified equation

$$\boldsymbol{I_D/I_G = C'(\lambda)\, L_a^2} \qquad (\mathbf{3})$$

where C (λ)', a new constant, was estimated to be 0.0055 for a laser wavelength λ = 514 nm when combining equations 2 and 3. From previous work[38],, graphitization is not achieved below ~1600 °C, therefore the crystallite size is not expected to evolve and be as large as for a fully graphitized structure (L_a > 2 nm). In this case L_a can be calculated by using Equation 3,

for which the in-plane crystalline size L_a < 2 nm. However, for the present work, the Raman spectra were obtained by using a 532 nm (2.33 eV) laser rather than a 514 nm wavelength source. The constant C' (λ = 532 nm) is therefore found to be 0.0062 (see Supplementary Information). [39] The relationship between I_D/I_G and L_a therefore obtained for L_a < 2 nm is

$$\boldsymbol{I_D/I_G = 0.0062\, L_a^2} \qquad (4)$$

The I_D/I_G ratio does not appear to change significantly, from 1.01 to 1.04 (Table S1), when growing CNTs on CNFs. This suggests that there is little change in the crystallinity of CF900/CNTs in comparison to CF900. In theory, a carbon fibre with a higher crystalline planar size L_a exhibits an improved graphitization degree and increased grain size, which results in stronger sp^2 carbon bonds and in turn improves the mechanical properties and electrical conductivity.[31]

A low intensity 2D band appears at ~2726 cm^{-1}, which is thought to arise from the presence of CNTs decorating the surface of the carbon fibres (see Figure 3b). The 2D-band is a second-order two-phonon process, and typical of all kinds of sp2 carbon materials including graphene, graphite and CNTs consist of ordered graphitic layers. Its intensity is sensitive to the number of graphene layers. Further evidence for this is obtained by the absence of this band for pure CF900. The full width at half maximum (FWHM) of a Raman peak is another indicator of crystallinity in carbonaceous materials. The FWHM of the D band in CF900 sharply decreases from 160 to 92 cm^{-1} after growth of the CNTs (see Table S1 in Supplementary Information). According to Ferrari,[40] a narrowing peak width reflects lower disorder, which indicates that the growth of CNTs leads to a higher crystalline structure of the CNF/CNTs composite fibres. This provides some evidence of an increasing overall crystallinity of the sample, but it is not conclusive given the lack of an increase in the I_D/I_G ratio. It could be that there is an averaging effect of the laser, whereby a broad distribution of material contributing to the intensities results, resulting in a smaller than expected change in this ratio.

3.3 Porosity Characterization

The N_2 adsorption/desorption isotherms of CF900 and CF900/CNTs are shown in Figure 4a. Both of the isotherms are Type H4 in accordance with IUPAC isotherms classification.[41] The isotherms experience a sharp increase at very low relative pressures, which indicates that both of the materials are dominated by micropores. The slight hysteresis loops of both isotherms

appear at P/P^0 of 0.4 - 0.5, suggesting the materials are micro-mesoporous. The N_2 adsorption plateaus when $P/P^0 > 0.5$, showing the materials have a very small amount of large mesopores and macropores.

As shown in Table 1, the CF900/CNTs exhibits a higher S_{BET} (1211 $m^2 g^{-1}$) and a total pore volume V_{tot} (0.53 $m^3 g^{-1}$) than CF900 with S_{BET} (712 $m^2 g^{-1}$) and V_{tot} (0.31 $m^3 g^{-1}$); this is considered to be attributed to the large surface area of CVD-grown CNTs. The value of S_{micro}/S_{BET} of both materials is greater than 80%, demonstrating that the specific surface area is mostly contributed by the presence of micropores. Both the V_{micro} and V_{meso} values are higher for the CF900/CNTs material compared to CF900. Moreover, the pore size distribution curves (Figure 4b) reveal that the pore size of both materials exhibit a range of sizes between 2 - 4 nm.

3.4 TGA analysis of the activated CNF/CNTs samples

A steady weight loss takes place from room temperature to 350 °C, which is attributed to the removal of moisture. A sharp weight loss is observed from 350 °C to 550 °C due to the degradation of CNFs and CNTs. The residue product comprising 14.6 wt.% is thought to be Fe_2O_3 after the CNFs/CNTs are completely burnt-off. The Fe nanoparticles in activated the CNF/CNTs then can be calculated to be 10.2 wt.% (2.4 mol. %).

3.5 Capacitance of the CNF/CNTs samples

Hierarchical CNF/CNTs composites, with good mechanical stability and electrical conductivity when connecting to the current collector, have been directly utilized as a supercapacitor electrode without any binder. Such a simplified route to fabricate a supercapacitor device has the advantage of improving capacitive performance by removing the poorly conducting binder and reducing the weight to volume ratio of the electrodes.

The CV curves obtained for the CF900 and CF900/CNTs electrodes at a scan rate of 10 mV s^{-1} exhibit a rectangular shape (Figure 6a), showing a typical behaviour seen previously for EDLC without obvious Faradaic reactions. The CF900/CNTs electrode has a larger CV bound area, and in turn a higher value of capacitance in comparison to the pristine CF900 electrode. The presence of CNTs on fibre surface results in a ~15% increase in the capacitance compared with the pristine fibres. This finding arises because the CNTs increase both the surface area and electrical conductivity of the electrode, giving rise to enlarged electrochemical active sites

with enhanced electron transport characteristics. It also important to mention the role of Fe catalysts in the growth of CNTs. The catalytic Fe nanoparticles diffuse into the electrospun carbon fibre substrate to form FeC_3 before the commencement of the nucleation of CNTs. Previous investigations have also observed inhomogeneous and very low-density CNTs growth on carbon fibre mats via CVD at 800 °C.[42] It has been suggested that it is more difficult to grow CNTs on carbon fibre substrates than on quartz. The proposed reason is that the catalytic nanoparticles readily react with carbon fibre matrices to form mixed sp^2-sp^3 carbons which result in a decreased number of catalytic nanoparticles remaining on the carbon fibre surface. In addition, a low yield of CNTs may also arise from the relatively small diameter of the electrospun carbon fibres. This potentially makes it difficult to provide large loading sites for catalytic nanoparticles on a single carbon fibre surface. However, to improve this situation, an introduction of reductive gas to keep the Fe nanoparticles from reacting with the carbon matrix or an application of a barrier coating on the carbon fibre surface can be used.[43] Therefore, an increased CNT growth could be optimised through this process but this is left as a future work objective.

In general, all the CV curves of CF900/CNTs obtained at different scan rates retain their rectangular shapes without obvious peaks (shown in Figure 6b). This indicates a good capacitive behaviour at a high scan rate. In addition, the slope of V/I yields the equivalent series resistance (R_s).[44] As the scan rate increases to 200 mV s^{-1}, the CV curves do not change shape, in which the slope of V/I undergoes a small change. This indicates our devices have a small R_s.

The comparison of GCD for the CF900, CF900/CNTs electrodes is presented in Figure 7a. At a low current density of 0.5 A g^{-1}, the performance of the electrodes is of the order of CF900/CNTs > CF900, which is consistent with their CV behaviour at a low scan rate. Specifically, the GCD curves at a current density of 0.5 A g^{-1} give capacitances of 149 and 131 F g^{-1} for CF900/CNTs and CF900, respectively. The capacitance increases by 15% from CF900 to CF900/CNTs due to the CNTs on the fibres' surface. Our results of capacitance are competitive compared to some of the latest biomass-based carbon supercapacitors, e.g. hemp-derived activated carbon (160 F g^{-1}),[45] rice husk based activated carbon (147 F g^{-1}),[46] starch-derived mesoporous carbon (144 F g^{-1}),[47] waste tea activated by K_2CO_3 or H_3PO_4 (203 F g^{-1} and 123 F g^{-1} respectively),[48] chlorella vulgaris based activated carbon (117 F g^{-1}),[49] and biomass-reed derived carbon nanosheet (147 F g^{-1}).[50] Also, our CNF/CNTs based electrodes

have exceed properties of cellulose/activated carbon composite materials (103.8 F g^{-1}).[51] On the other hand, the capacitance of our devices are not as high as some other biomass based supercapacitors, e.g. sawdust (242 F g^{-1}),[52] wood sawdust (225 F g^{-1}),[53] coconut fibres (266 F g^{-1}),[54] waste cotton glove (218 F g^{-1}),[55] pineapple leaf fibre (202 F g^{-1}),[56] lignin (226 F g^{-1}).[57] Some strategies could be adopted in order to improve the performance by optimizing parameters of electrospinning, carbonization and activation temperature, and removing impurities in CNFs/CNTs. The performance of our materials are not the highest, yet they are comparable with the state-of-the-art supercapacitors. However, they have their own advantages compared to other systems. In our study, we have applied a relatively easy and cheap approach to grow CNTs. This is due to the fact that the floating catalytic CVD process is a one-step method to produce CNTs, which allows this method to be scaled-up. To further develop the productivity, needless electrospinning[58] and multi-needle electrospinning[59] could also be applied to produce cellulose fibres. Taken as a value normalised to the surface area we obtain values of 100 mF cm^{-2} and 170 mF cm^{-2} for the CF900 to CF900/CNTs samples respectively. The areal specific capacitances of our electrode materials are competitive with the other carbon-based electrodes, e.g. coaxial carbon fibre,[60] ZnO activated carbon textile,[61] carbon nanosheets coated carbon fibre,[62] and even carbon nanoparticles/MnO_2 nanorods for pseudocapacitors.[63] In addition to CF900, the CNTs that have grown on the surface of CF900 are also activated by KOH. The specific capacitance of the activated pure MWCNTs could experience a 5 - fold increase in comparison to the original MWCNTs. This development of high capacitive performance results from the generation of micropores on the CNTs' graphitic walls.[64] The microporous structure of CNTs with large reactive sites and their highly conductive properties are attributed to the adsorption of a large number of ions on to the electrodes, leading to a higher capacitance in CF900/CNTs. The specific capacitance obtained for CF900/CNTs is competitive with previous work with cellulose precursors, in which they produced electrode materials by directly electrospinning a mixed solution of 6 wt.% CNTs with a cellulose precursor.[14] The increase in capacitance was attributed to the presence of CNTs protruding from the fibre surface.[14] The presence of such CNTs protruding from the surface was however serendipitous. Here we obtain the same result by an alternative route. The availability of the CNTs at the surface could allow for the coupling of these devices to a solid matrix dielectric, obtaining a structural capacitor, the subject of which has been recently reviewed.[16]

The GCD curves for CF900/CNTs (Figure 7b) at different current densities show an almost symmetrical triangular shape with small voltage drops at the initial point of the discharge curve (0.032 V at a current density of 10 A g^{-1}), indicating a low R_s of the device. This triangular shape is retained at a higher current density of 10 A g^{-1}, showing an excellent capacitive behaviour of the electrode.

As can be seen from Figure 7c, as the current density increases from 0.5 to 10 A g^{-1}, the capacitance of both materials decreases. In general, a low scan rate (0.5 A g^{-1}) results in a slow mobility of the electrolyte ions, allowing them to have enough time to diffuse into the available reactive sites of the electrodes. However, at higher scan rates (10 A g^{-1}), the electrolyte ions can only approach the surface of the electrode rather than access into the porous structure, therefore negatively influencing of capacitive behaviour.[65] In addition, the capacitances of CF900/CNTs at all the current densities are higher than those of CF900 counterpart, which confirms that the growth of CNTs improves the capacitive performance. It is also noted that a greater increase in capacitance by virtue of the growth of CNTs is observed at a high current density of 10 A g^{-1}. Specifically, although the capacitance of CF900/CNTs increased by 15% at a current density of 0.5 A g^{-1} in comparison to CF900, a 22% improvement is noted at a current density of 10 A g^{-1}. When increasing to a higher current density of 10 A g^{-1}, the specific capacitance retains 84% and 90% of its initial value for the CF900 and CF900/CNTs samples respectively. The improvement of rate capability from CF900 to CF900/CNTs suggests the growth of CNTs enhances the electrical conductivity performance to accelerate the electron transfer.

The EIS profiles exhibit behaviour of a supercapacitor with a porous carbon fibre electrode (Figure 8). The equivalent circuit model is presented in the inset, which includes equivalent series resistance (R_s), charge transfer resistance (R_{ct}), Warburg resistance (Z_w), double layer capacitance (C). Table 2 shows the resistance parameters of both electrodes. In the Nyquist plot, the R_s of a system is defined as the initial intercept of the semicircle with the Z'-axis in the high frequency region. In accordance to EIS, the CF900, CF900/CNTs samples have small R_s values (0.69 and 0.27 $\Omega \cdot cm^2$, respectively). This shows the growth of CNTs results in a decrease of R_s, which increases the electron transport properties of the electrodes. The R_{ct} at the electrolyte/electrode interfaces can be expressed as the intercept of the semicircle in the mid-to-high frequency region. The charge transfer resistance results from the movement of charge close to the Helmholtz plane.[66] It is noted that R_{ct} is lower for the CF900/CNTs (1.30

$\Omega \cdot cm^2$) electrode in comparison to the CF900 electrode (1.35 $\Omega \cdot cm^2$); the growth of CNTs on CF900 lowers the R_{ct}. At a 45° region in the Nyquist plot, known as the Warburg region; the slope of this portion of the curve is called the Warburg resistance (Z_w) and is a result of the frequency dependence of ion diffusion/transport in the electrolyte.[60] Normally the vertical line represents the formation of an ideal capacitor. However, from the Nyquist plot the present supercapacitors are controlled by both kinetic and diffusion processes. The reason for this may arise from the existence of iron nanoparticles which can influence the diffusion process. The Warburg resistance of CF900/CNTs (4.59 $\Omega \cdot cm^2$) is higher than that of CF900 (3.78 $\Omega \cdot cm^2$). This is indicative of a shorter ion diffusion path for CF900/CNTs, resulting in a faster mobility of ions compared to CF900.[67] A more comprehensive analysis of all relevant impedance parameters, including resistance of electrolyte, R_{ct} and Warburg impedance, can be done using an equivalent circuit.

Repetitive charge/discharge tests for the CF900 and CF900/CNTs-based devices were performed at a current density of 2 A g^{-1} for 1000 cycles to assess their cyclic performance (Figure 9). Both of the CF900 and CF900/CNTs samples retain 90% of the capacitance of their initial values after 1000 cycles, which shows the excellent stability and lifetime of both devices.

4. Conclusions

Hierarchical cellulose based CNF/CNTs composite fibres were produced by growing CNTs on the surface of electrospun CNFs using a floating catalyst CVD process. A CVD temperature of 800 °C has been shown to be optimal to grow pure CNTs without the formation of amorphous carbons. The specific capacitance for samples with grown CNTs on the surface achieved a high value 149 F g^{-1} (170 mF cm^{-2}) at a current density 0.5 A g^{-1}, an increase of 15% compared to the neat CNF counterpart. The growth of CNTs improves the electrochemical performance by lowering the R_s, R_{ct}, and Z_w of the electrodes. The hierarchical CNF/CNTs composite can retain ~90% of its initial capacitance after being cycled 1000 times at 2 A g^{-1}, exhibiting a good stability. This is thought to be due to the fact that the growth of CNTs enlarges the reactive sites through enhanced surface area and porosity Accordingly, the BET specific surface area increases from 712 $m^2 g^{-1}$ to 1211 $m^2 g^{-1}$, while the pore volume increases from 0.31 to 0.53 $m^3 g^{-1}$ after the growth of CNTs. There is some evidence that the growth of CNTs on the CNF also leads to a higher degree of overall crystallinity to improve the conductivity of CNF, which has been demonstrated by Raman spectroscopic analysis. The cellulose-based CNF/CNTs

composite material has been demonstrated to be an excellent electrode to manufacture high-performance supercapacitors.

Acknowledgements

The authors would like to thank the Chinese Scholarship Council and the University of Exeter for funding a studentship (for Q.L.).

Supplementary Information

Figure S1 Image of a coin cell supercapacitor; Derivation of the relationship between I_D/I_G and L_a; Table S1, Peak frequencies, intensity ratios (I_D/I_G), and FWHM of Raman D and G bands for CF900 and CF900/CNTs

Table S1 Peak frequencies, intensity ratios (I_D/I_G), and FWHM of Raman D and G band for CF900 and CF900/CNTs

(a)

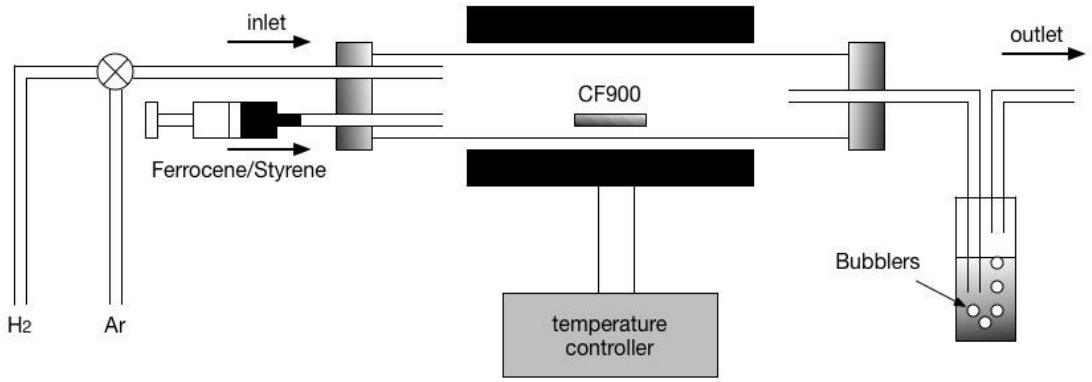

(b)

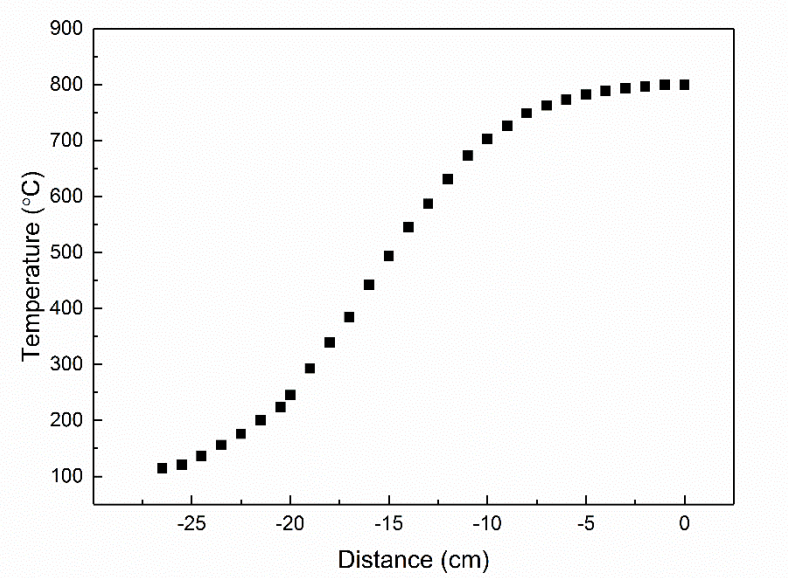

Figure 1 (a) A schematic of the CVD procedure for the CNT growth on the CNF mat. (b) The temperature versus distance profile from the syringe end to the centre of the hot reaction zone. The length of the reaction zone is 4 cm in total.

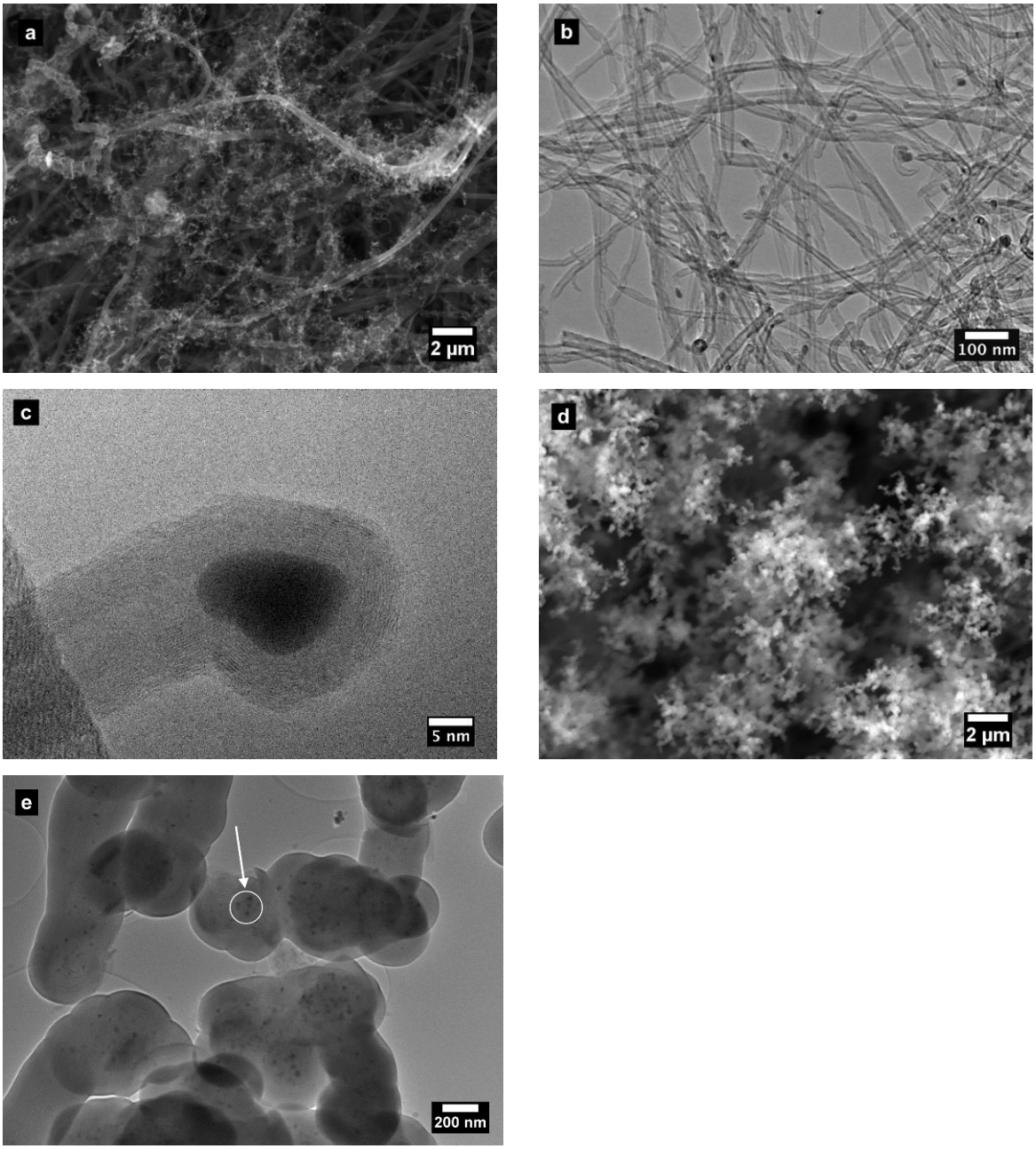

Figure 2 (a) SEM image of CNTs grown on the surface of CNFs at a CVD temperature of 800 °C; (b) TEM image of a CNT grown from CNFs with an Fe nanoparticle at the tip at a CVD temperature of 800 °C; (c) magnified TEM image of (b); (d) SEM image of the mixture of amorphous carbon and CNTs grown at a CVD temperature of 900 °C; (e) TEM image of amorphous carbon with the Fe nanoparticles (white arrow) at a CVD temperature of 900 °C.

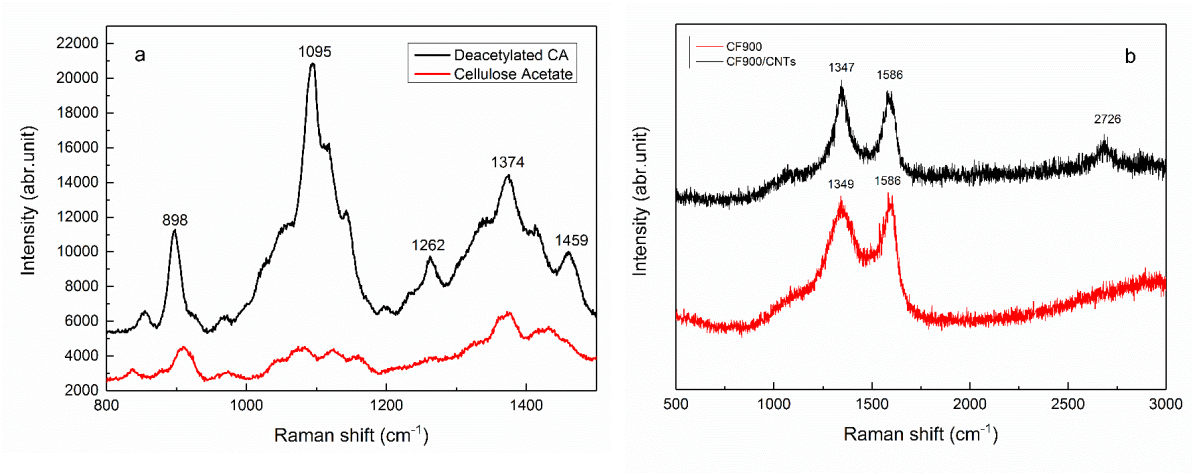

Figure 3 Typical (a) Raman spectra of the cellulose acetate (CA) and deacetylated CA fibres and (b) Raman spectra of CF900 and CF900/CNTs samples.

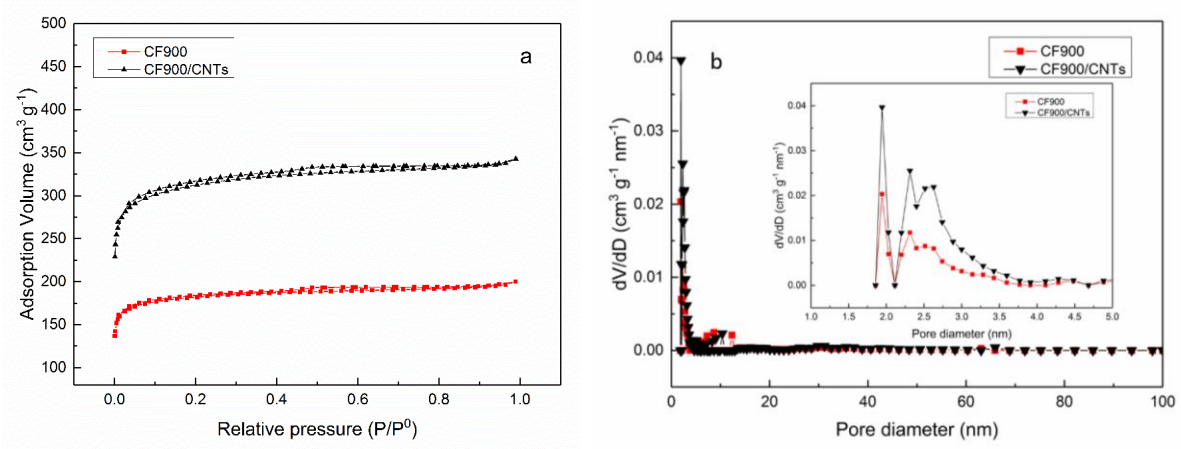

Figure 4 Typical (a) isotherms of CF900 and CF900/CNTs and (b) pore size distribution of CF900 and CF900/CNTs.

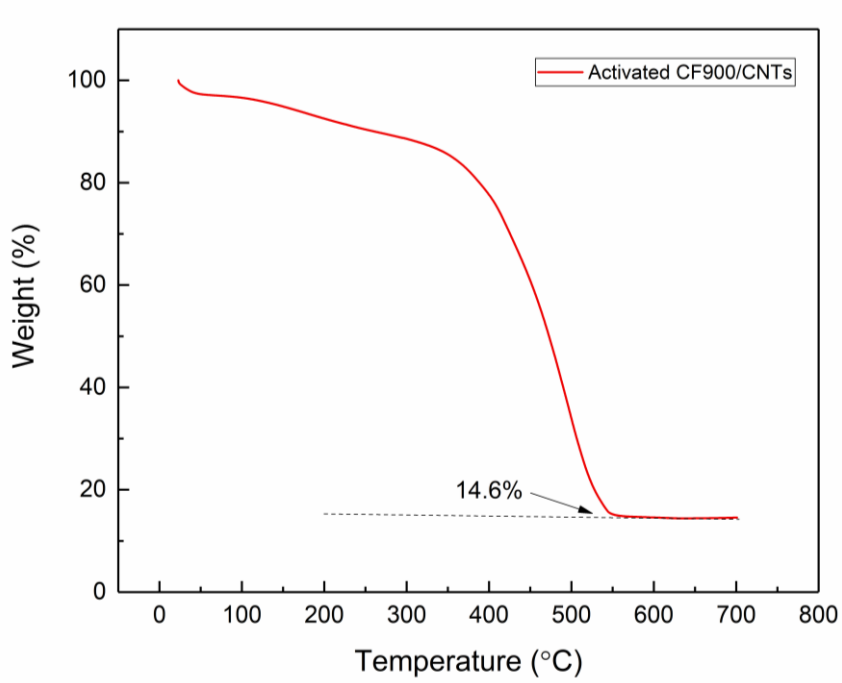

Figure 5 TGA for CF900/CNTs obtained at temperature heating from room temperature to 700 °C

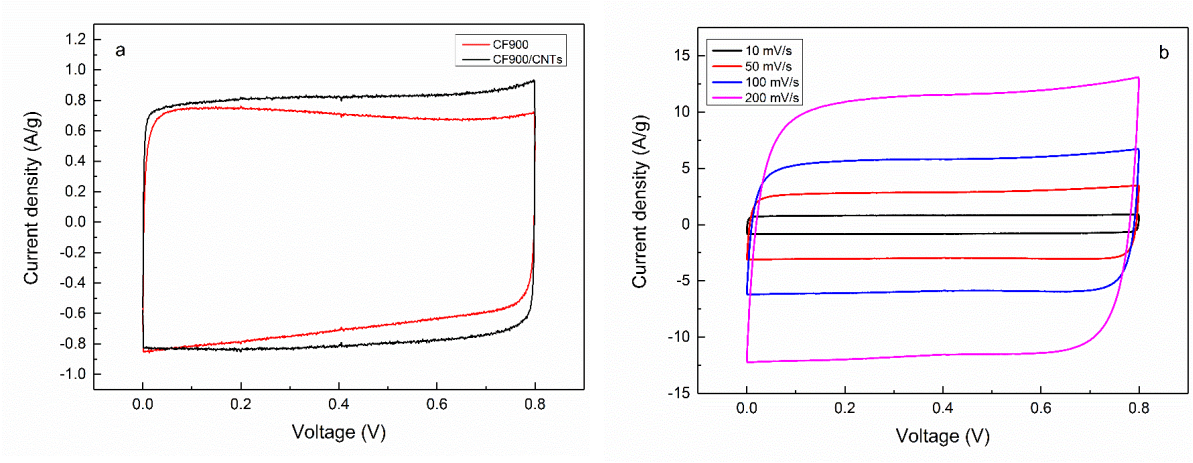

Figure 6 (a) CV curves of CF900 and CF900/CNTs at a scan rate of 10 mV s^{-1}; (b) CV curves of CF900/CNTs obtained at a scan rate ranging from 10 to 200 mV s^{-1}.

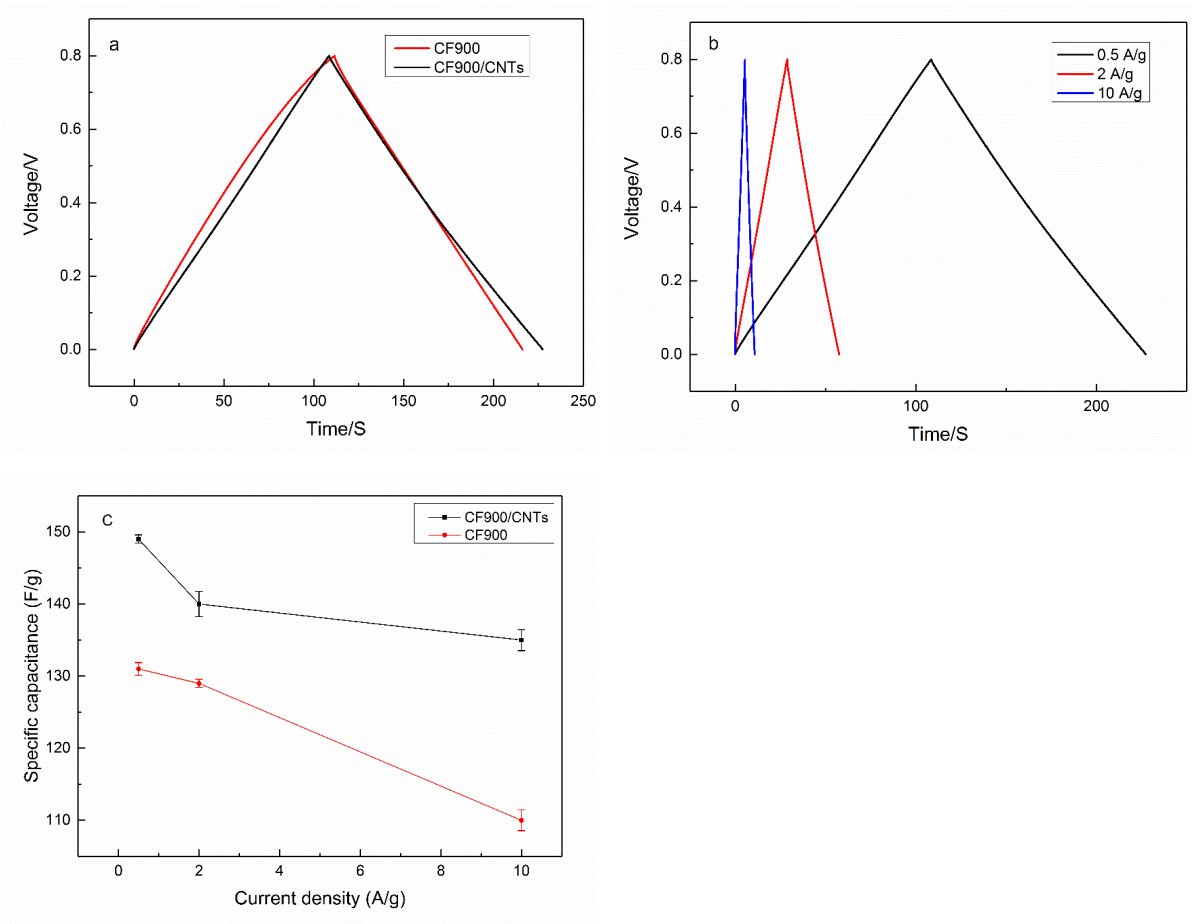

Figure 7 (a) Charge/discharge curves obtained at a current density of 0.5 A g^{-1} for CF900, and CF900/CNTs electrodes; (b) Charge/discharge curves obtained at current densities ranging from 0.5 to 10 A g^{-1} for CF900/CNTs electrodes; (c) Specific capacitances of the CF900 and CF900/CNTs electrodes as a function of the current density.

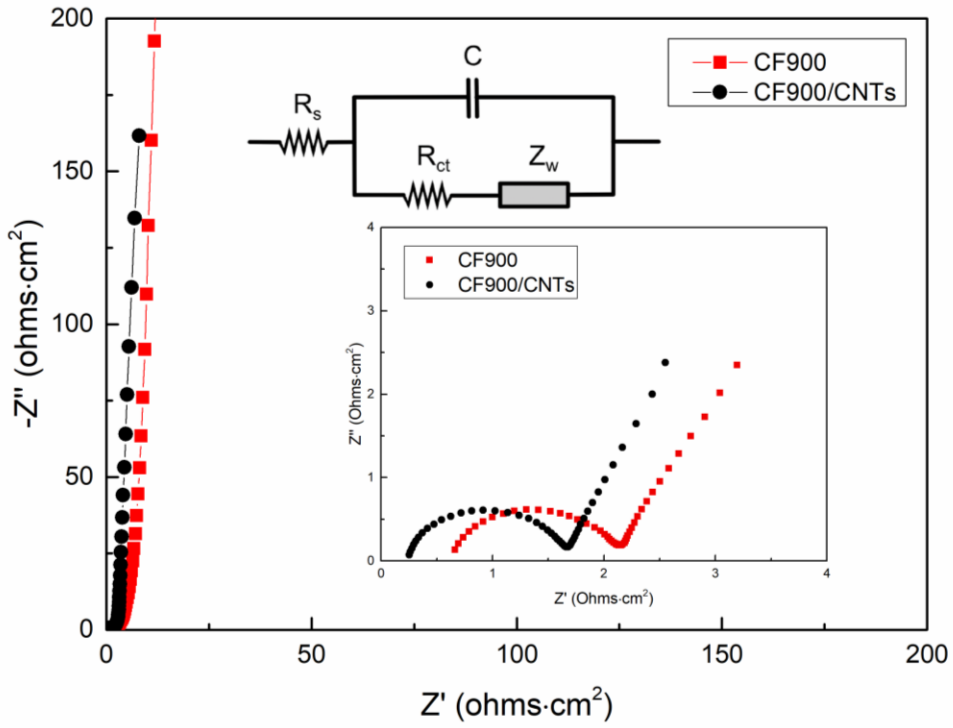

Figure 8 EIS curves for the CF900, CF900/CNTs samples.

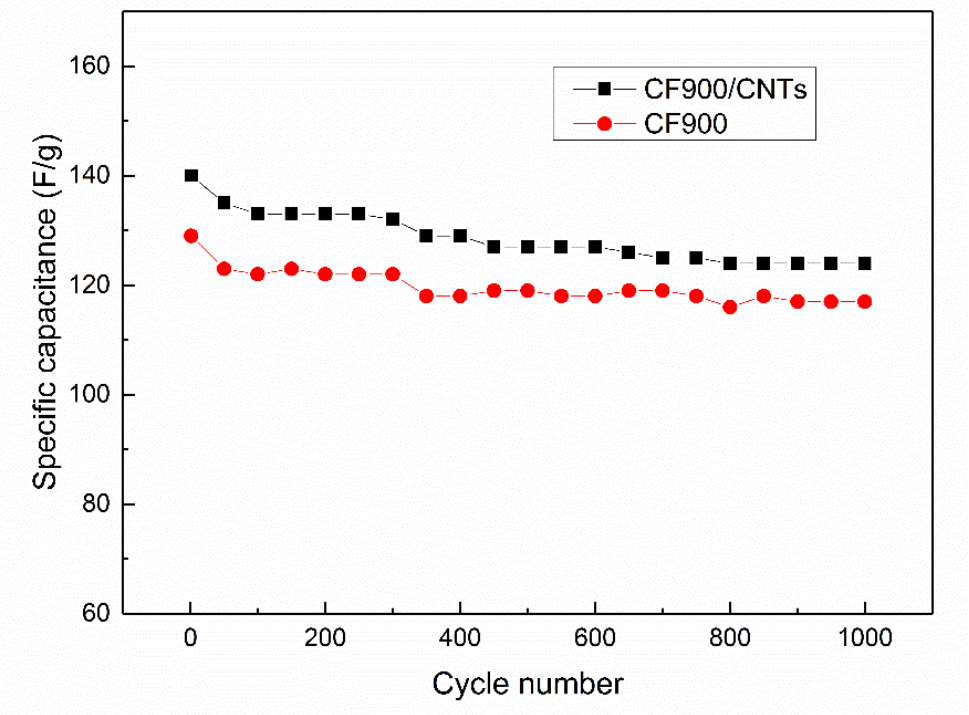

Figure 9 Cycling performance of the electrodes over 1000 cycles at a constant current density of 2 A g^{-1} for CF900 and CF900/CNTs.

Table 1 Pore properties of CF900 and CF900/CNTs

	S_{BET} ($m^2\ g^{-1}$)	S_{micro} ($m^2\ g^{-1}$)	S_{meso} ($m^2\ g^{-1}$)	V_{tot} ($m^3\ g^{-1}$)	V_{micro} ($m^3\ g^{-1}$)	V_{meso} ($m^3\ g^{-1}$)
CF900	712	611	63	0.31	0.24	0.05
CF900/CNTs	1211	1001	131	0.53	0.39	0.10

Table 2 Impedance parameters for CF900 and CF900/CNTs.

Electrodes	$R_s/\Omega\cdot cm^2$	$R_t/\Omega\cdot cm^2$	$Z_W/\Omega\cdot cm^2$
CF900	0.69 ± 0.009	1.35 ± 0.014	4.59 ± 0.223
CF900/CNTs	0.27 ± 0.004	1.30 ± 0.010	3.78 ± 0.155

References

1. Z. N. Yu, L. Tetard, L. Zhai, and J. Thomas, *Energ Environ Sci*, **8**, 702 (2015).

2. A. Gonzalez, E. Goikolea, J. A. Barrena, and R. Mysyk, *Renew Sust Energ Rev,* **58** 1189 (2016).

3. M. Salanne, B. Rotenberg, K. Naoi, K. Kaneko, P. L. Taberna, C. P. Grey, B. Dunn, and P. Simon, *Nature Energy*, **1**, 16070 (2016).

4. E. Frank, L. M. Steudle, D. Ingildeev, J. M. Sporl, and M. R. Buchmeiser, *Angew. Chem.-Int. Edit.,* **53**, 5262 (2014).

5. A. G. Dumanlı and A. H. Windle, *J Mater Sci*, **47**, 4236 (2012).

6. C. L. Zhang and S. H. Yu, *Chem Soc Rev,* **43**, 4423 (2014).

7. B. Sun, Y. Z. Long, H. D. Zhang, M. M. Li, J. L. Duvail, X. Y. Jiang, and H. L. Yin, *Prog Polym Sci*, **39**, 862 (2014).

8. B. Zhang, F. Kang, J.-M. Tarascon, and J.-K. Kim, *Progress in Materials Science*, **76**, 319 (2016).

9. S. Iijima, *Nature*, **354**, 56 (1991).

10. Q. Zheng, Z. Cai, Z. Ma, and S. Gong, *ACS Appl. Mater. Interfaces*, **7**, 3263 (2015).

11. T. Wang, D. F. Song, H. Zhao, J. Y. Chen, C. H. Zhao, L. L. Chen, W. J. Chen, J. Y. Zhou, and E. Q. Xie, *J Power Sources*, **274** 709 (2015).

12. J. Yu, W. Lu, S. Pei, K. Gong, L. Wang, L. Meng, Y. Huang, J. P. Smith, K. S. Booksh, Q. Li, J. H. Byun, Y. Oh, Y. Yan, and T. W. Chou, *ACS Nano*, **10**, 5204 (2016).

13. F. J. Miao, C. L. Shao, X. H. Li, K. X. Wang, N. Lu, and Y. C. Liu, *ACS Sustain Chem Eng*, **4**, 1689 (2016).

14. L. Deng, R. J. Young, I. A. Kinloch, A. M. Abdelkader, S. M. Holmes, D. A. De Haro-Del Rio, and S. J. Eichhorn, *ACS Appl. Mater. Interfaces*, **5**, 9983 (2013).

15. H. Qian, H. Diao, N. Shirshova, E. S. Greenhalgh, J. G. H. Steinke, M. S. P. Shaffer, and A. Bismarck, *Journal of Colloid and Interface Science,* **395**, 241 (2013).

16. H. Qian, E. S. Greenhalgh, M. S. P. Shaffer, and A. Bismarck, *J Mater Chem,* **20**, 4751 (2010).

17. M. S. Islam, Y. Deng, L. Y. Tong, S. N. Faisal, A. K. Roy, A. I. Minett, and V. G. Gomes, *Carbon,* **96**, 701 (2016).

18. M. A. Shazed, A. R. Suraya, S. Rahmanian, and M. A. M. Salleh, *Mater Design,* **54**, 660 (2014).

19. R. Samsur, V. K. Rangari, S. Jeelani, L. Zhang, and Z. Y. Cheng, *J Appl Phys,* **113**, 214903 (2013).

20. H. Q. Hou and D. H. Reneker, *Adv Mater,* **16**, 69 (2004).

21. C. Lai, Q. Guo, X. F. Wu, D. H. Reneker, and H. Hou, *Nanotechnology,* **19**, 195303 (2008).

22. S. Abouali, M. Akbari Garakani, B. Zhang, Z.-L. Xu, E. Kamali Heidari, J.-q. Huang, J. Huang, and J.-K. Kim, *ACS Applied Materials & Interfaces,* **7**, 13503 (2015).

23. I. Kunadian, R. Andrews, D. L. Qian, and M. P. Menguc, *Carbon,* **47**, 384 (2009).

24. A. Bhattacharjee, A. Rooj, D. Roy, and M. Roy, *Journal of Experimental Physics,* **513268** 1-8 (2014).

25. S. Zhu, C. H. Su, S. L. Lehoczky, I. Muntele, and D. Ila, *Diam Relat Mater,* **12**, 1825 (2003).

26. R. Andrews, D. Jacques, D. Qian, and T. Rantell, *Acc Chem Res,* **35**, 1008 (2002).

27. Q. H. Zhang, J. W. Liu, R. Sager, L. M. Dai, and J. Baur, *Compos Sci Technol,* **69**, 594 (2009).

28. L. B. Deng, R. J. Young, I. A. Kinloch, Y. Q. Zhu, and S. J. Eichhorn, *Carbon,* **58**, 66 (2013).

29. K. Kavkler and A. Demsar, *Spectrochim Acta A Mol Biomol Spectrosc*, **78**, 740 (2011).

30. J. H. Wiley and R. H. Atalla, *Carbohydrate Research*, **160**, 113 (1987).

31. M. A. Pimenta, G. Dresselhaus, M. S. Dresselhaus, L. G. Cancado, A. Jorio, and R. Saito, *Phys Chem Chem Phys*, **9**, 1276 (2007).

32. A. C. Ferrari, J. C. Meyer, V. Scardaci, C. Casiraghi, M. Lazzeri, F. Mauri, S. Piscanec, D. Jiang, K. S. Novoselov, S. Roth, and A. K. Geim, *Phys Rev Lett*, **97**, 187401 (2006).

33. J. H. Lehman, M. Terrones, E. Mansfield, K. E. Hurst, and V. Meunier, *Carbon*, **49**, 2581 (2011).

34. L. Bokobza and J. Zhang, *Express Polym Lett*, 6 (7), 601-608 (2012).

35. F. Tuinstra and J. L. Koenig, *The Journal of Chemical Physics*, 53 (3), 1126-1130 (1970).

36. A. C. Ferrari and J. Robertson, *Phys Rev B*, 61 (20), 14095-14107 (2000).

37. L. G. Cancado, K. Takai, T. Enoki, M. Endo, Y. A. Kim, H. Mizusaki, A. Jorio, L. N. Coelho, R. Magalhaes-Paniago, and M. A. Pimenta, *Appl Phys Lett*, **88**, 163106 (2006).

38. K. Kong, L. B. Deng, I. A. Kinloch, R. J. Young, and S. J. Eichhorn, *J Mater Sci*, **47**, 5402 (2012).

39. M. J. Matthews, M. A. Pimenta, G. Dresselhaus, M. S. Dresselhaus, and M. Endo, *Phys Rev B*, **59**, R6585-R6588 (1999).

40. A. C. Ferrari, *Solid State Commun*, **143**, 47-57 (2007).

41. M. Thommes, K. Kaneko, A. V. Neimark, J. P. Olivier, F. Rodriguez-Reinoso, J. Rouquerol, and K. S. W. Sing, *Pure and Applied Chemistry*, **87**, 1051 (2015).

42. N. Sonoyama, M. Ohshita, A. Nijubu, H. Nishikawa, H. Yanase, J. Hayashi, and T. Chiba, *Carbon*, **44**, 1754 (2006).

43. S. A. Steiner, 3rd, R. Li, and B. L. Wardle, *ACS Appl. Mater. Interfaces*, **5**, 4892 (2013).

44. Q. H. Guo, X. P. Zhou, X. Y. Li, S. L. Chen, A. Seema, A. Greiner, and H. Q. Hou, *J Mater Chem*, **19**, 2810 (2009).

45. W. Sun, S. M. Lipka, C. Swartz, D. Williams, and F. Q. Yang, *Carbon*, **103** 181 (2016).

46. E. Y. L. Teo, L. Muniandy, E. P. Ng, F. Adam, A. R. Mohamed, R. Jose, and K. F. Chong, *Electrochim Acta*, **192** 110 (2016).

47. M. B. Wu, P. P. Ai, M. H. Tan, B. Jiang, Y. P. Li, J. T. Zheng, W. T. Wu, Z. T. Li, Q. H. Zhang, and X. J. He, *Chem Eng J*, **245** 166 (2014).

48. I. I. G. Inal, S. M. Holmes, A. Banford, and Z. Aktas, *Appl Surf Sci*, **357** 696 (2015).

49. K. S. Lee, M. Park, C. W. Park, and J. D. Kim, *Coll Surf A*, 529 102 (2017).

50. D. Zhou, H. Wang, N. Mao, Y. Chen, Y. Zhou, T. Yin, H. Xie, W. Liu, S. Chen, and X. Wang, *Micropor Mesopor Mat*, **241** 202 (2017).

51. K. Murashko, D. Nevstrueva, A. Pihlajamaki, T. Koiranen, and J. Pyrhonen, *Energy*, **119** 435 (2017).

52. Y. X. Huang, Y. Liu, G. J. Zhao, and J. Y. Chen, *J Mater Sci*, **52**, 478 (2017).

53. Y. Huang, L. Peng, Y. Liu, G. Zhao, J. Y. Chen, and G. Yu, *ACS Appl Mater & Interf*, **8**, 15205 (2016).

54. L. H. Yin, Y. Chen, D. Li, X. Q. Zhao, B. Hou, and B. K. Cao, *Mater Design*, **111** 44 (2016).

55. C. Wei, J. L. Yu, X. Q. Yang, and G. Q. Zhang, *Nano Res Lett*, **12**, 379 (2017).

56. J. Sodtipinta, C. Ieosakulrat, N. Poonyayant, P. Kidkhunthod, N. Chanlek, T. Amornsakchai, and P. Pakawatpanurut, *Ind Crops & Prod*, **104** 13 (2017).

57. S. Hu and Y.-L. Hsieh, *RSC Adv*, **7**, 30459 (2017).

58. W. E. Teo and S. Ramakrishna, *Nanotech*, **17**, R89 (2006).

59. L. Persano, A. Camposeo, C. Tekmen, and D. Pisignano, Macromol Mater & Eng, **298** , 504 (2013).

60. V. T. Le, H. Kim, A. Ghosh, J. Kim, J. Chang, Q. A. Vu, D. T. Pham, J. H. Lee, S. W. Kim, and Y. H. Lee, *ACS Nano*, **7**, 5940 (2013).

61. D. V. Lam, K. Jo, C. H. Kim, J. H. Kim, H. J. Lee, and S. M. Lee, *ACS Nano*, **10**, 11351 (2016).

62. X. Zhao, H. Tian, M. Y. Zhu, K. Tian, J. J. Wang, F. Y. Kang, and R. A. Outlaw, *J Power Sources*, **194**, 1208 (2009).

63. L. Y. Yuan, X. H. Lu, X. Xiao, T. Zhai, J. J. Dai, F. C. Zhang, B. Hu, X. Wang, L. Gong, J. Chen, C. G. Hu, Y. X. Tong, J. Zhou, and Z. L. Wang, *ACS Nano*, **6**, 656 (2012).

64. E. Frackowiak, S. Delpeux, K. Jurewicz, K. Szostak, D. Cazorla-Amoros, and F. Beguin, *Chemical Physics Letters*, **361**, 35 (2002).

65. M. Fatnassi and M. Es-Souni, *Rsc Adv*, **5**, 21550 (2015).

66. K. S. Hung, C. Masarapu, T. H. Ko, and B. Q. Wei, *J Power Sources*, **193**, 944 (2009)

67. D. Zhang, X. Zhang, Y. Chen, P. Yu, C. Wang, and Y. Ma, *J Power Sources*, **196**, 5990 (2011).